

# Chaos in the general relativistic Poynting-Robertson effect: Kerr equatorial plane

Vittorio De Falco<sup>1\*</sup>

<sup>1</sup> *Research Centre for Computational Physics and Data Processing,  
Faculty of Philosophy & Science, Silesian University in Opava,  
Bezručovo nám. 13, CZ-746 01 Opava, Czech Republic  
(Dated: March 14, 2022)*

We apply the Melnikov method to prove that under the general relativistic Poynting-Robertson (PR) effect-perturbations the homoclinic orbits in the equatorial plane of Kerr spacetime become chaotic. The proof mainly reduces to see whether a  $g$  function, depending on Kerr spin  $a$ , periastron of the homoclinic orbit  $r_u$ , and radius and angular velocity  $(R_*, \Omega_*)$  of the radiation source, admits simple zeros with respect to the radial coordinate  $r$ , ranging between  $r_u$  and the apastron  $r_a$  of the homoclinic orbit. The set of parameters, which shows a chaotic behavior, forms what we call the “chaotic region” in the parameter space. We give an estimated numerical definition of such region, because the non-linear dependence of the  $g$  function from these parameters makes hard to develop an analytical treatment. We finally discuss about the obtained results and future developments.

## 1. INTRODUCTION

Chaos is a widespread feature in most of physical non-linear dynamical systems. The term “chaos” can apparently refer to something which is structureless or a state of disorder and is often associated to the concept of highly-sensitivity to the initial conditions. Edward Lorenz defined the chaos as: “*when the present determines the future, but the approximate present does not approximately determine the future.*” Although there exists no universally accepted formal definition of chaos (long-standing and still modern issue), the most common used is the one due to Robert L. Devaney, who states that a dynamical system is chaotic if it fulfills the following proprieties [1]: (1) *sensitive dependence on initial conditions* (tiny perturbations on the initial conditions may lead to significantly different future behaviors), (2) *topologically mixing* (any given region or open set of the phase space eventually overlaps with any other given region), (3) *presence of dense periodic orbits* (every point in the space is approached arbitrarily close by periodic orbits).

A formal treatment of chaos is extremely important because it hides behind the visible randomness of chaotic complex dynamics, some underlying rich mathematical structures, such as: constant feedback loops, self-similarity, fractals, and self-organization [2, 3]. In this paper, we limit our attention to classical deterministic-chaotic systems, where *deterministic* means that the future behavior of a system is fully determined by their initial conditions, with no noise, randomness, or probabilities built in. The repeated application of a non-linear function on the initial conditions generates a quite complicated long-term behavior, where in this sense, the unpredictability emerges over time. There are however other approaches dealing also with semiclassical and quantum chaos (see Refs. [4–7], for more details).

Several different classical methods have been developed to identify chaos, which may manifest globally or on some particular subsets of the phase space. We briefly recall some of the most common [3, 5, 8], like: Poincaré surface of section, Kolmogorov-Arnold-Moser (KAM) theory, bifurcation theory, symbolic dynamics, Lyapunov exponent, Poincaré-Birkhoff fixed point theorem, power spectra, hyperbolic invariant sets and homoclinic points.

General Relativity (GR), being a non-linear theory, can potentially manifest chaotic behaviors [9]. It has been proved that some relativistic dynamical system show chaotic features, obtaining also several important results. These studies can be mainly divided in two branches: problems of geodesic or non-geodesic motion of a particle in a given gravitational field and evolution of cosmological models. Regarding works on the first class, it is important to cite: the motion in spaces with negative curvature [10], motion around two fixed black holes (BHs) [9, 11, 12], relativistic restricted three-body problem [13], Schwarzschild BH affected by high-frequency periodic perturbations [14], spinning particle motion around a Kerr and Schwarzschild BH [15, 16], gravitational waves from spinning compact binaries [17–19]. Instead, about chaos in cosmology it is worth to mention: Bianchi IX (“mixmaster”) [20–22], Friedmann-Robertson-Walker (FRW) [23], and the non-linear interaction among dark matter, dark energy, matter and radiation on FRW spacetime [24].

In this paper, we focus our attention on the *general relativistic PR effect in the equatorial plane around a Kerr compact object*. In high-energy astrophysics, when we deal with electromagnetic radiation processes around compact objects, like neutron stars (NSs) or BHs, relatively small-sized test particles can drastically depart from their geodesic motion. The gravitational pull is contrasted by the radiation pressure, and in the process of absorption and remission of radiation from the test particle, there is also the radiation drag force, opposite to the test particle orbital motion [25, 26]. The PR effect con-

\* vittorio.defalco@physics.cz

figures thus as a pure relativistic dissipative effect, which efficiently removes energy and angular momentum from the affected test particle. The general relativistic treatments in Kerr spacetime have been proposed from the two dimensional (2D) [27, 28] until the three dimensional (3D) formulations [29–31]. They all show a common feature, namely the existence of a critical hypersurface, region where gravitational and radiation forces balance and the test particle moves on it stably.

Such system has never been analysed under a dynamical system point of view, which could go beyond the stability of the critical hypersurfaces [28, 32]. In general, the methods for identifying chaos in a relativistic dynamical system are widely based on those of classical physics, and then improved and adapted for GR theory. In our study, we apply the *Melnikov method* [2, 8], well known in the GR literature (see e.g., Refs. [14, 15]). This is an independent diagnostic procedure, complementary to other numerical and analytical methods. Its strength relies on the fact, that *it requires only the knowledge of invariant subsets in the phase space of the unperturbed dynamics (homoclinic orbits), and of the explicit expression of the perturbations, without knowing the solution of the perturbed dynamics*. In addition, it search for particular structures in the phase space, namely the *Smale horse-shoes*, which are sirens of chaotic behavior and posses a Cantor set structure. Therefore, it is able to provide more accurate information concerning the type of behavior of the perturbed dynamics with respect to other methods.

This work provides a self-consistent introduction to the arguments, addressing the reader to precise references for more details. The paper is organized as follows: in Sec. 2 we recall the general relativistic PR effect model; in Sec. 3 we derive the Hamiltonian formulation of the general relativistic PR effect; in Sec. 4 we describe the homoclinic orbits in the equatorial plane of the Kerr spacetime; in Sec. 5 we recall the Melnikov method and then we apply it to the general relativistic PR effect; in Sec. 6 we discuss about the obtained results. Finally, in Sec. 7 we draw our conclusions.

## 2. GENERAL RELATIVISTIC PR EFFECT MODEL

We consider a central compact object, whose outside spacetime is described by the Kerr metric with signature  $(-, +, +, +)$ . In geometrical units ( $c = G = 1$ ), the line element of the Kerr spacetime,  $ds^2 = g_{\alpha\beta} dx^\alpha dx^\beta$ , in Boyer-Lindquist coordinates, parameterized by mass  $M$  (set equal to unity,  $M = 1$ ) and spin  $a$ , set in the equatorial plane  $\theta = \pi/2$ , reads as

$$ds^2 = \left(\frac{2}{r} - 1\right) dt^2 - \frac{4a}{r} dt d\varphi + \frac{r^2}{\Delta} dr^2 + \rho d\varphi^2, \quad (1)$$

where  $\Delta \equiv r^2 - 2r + a^2$ , and  $\rho \equiv r^2 + a^2 + 2a^2/r$ . We introduce the zero angular momentum observers (ZAMOs),

whose adapted orthonormal frame is given by

$$\begin{aligned} e_{\hat{t}} &\equiv \mathbf{n} = \frac{1}{N}(\partial_t - N^\varphi \partial_\varphi), \\ e_{\hat{r}} &= \frac{1}{\sqrt{g_{rr}}} \partial_r, \quad e_{\hat{\varphi}} = \frac{1}{\sqrt{g_{\varphi\varphi}}} \partial_\varphi, \end{aligned} \quad (2)$$

where  $\{\partial_t, \partial_r, \partial_\varphi\}$  is the orthonormal frame adapted to the static observer at infinity,  $N = (-g^{tt})^{-1/2}$  is the time lapse function and  $N^\varphi = g_{t\varphi}/g_{\varphi\varphi}$  the spatial shift vector field. All the vector and tensor indices (e.g.,  $v^\alpha, T^{\alpha\beta}$ ) associated to the ZAMO frame will be labeled by a hat (e.g.,  $v^{\hat{\alpha}}, T^{\hat{\alpha}\hat{\beta}}$ ), instead all the scalar quantities measured in the ZAMO frame (e.g.,  $f$ ) will be followed by  $(n)$  (e.g.,  $f(n)$ ). In the kinematical decomposition of the ZAMO congruence, we have that the nonzero ZAMO kinematical quantities are acceleration  $\mathbf{a}(n) = \nabla_{\mathbf{n}} \mathbf{n}$ , expansion tensor along the  $\hat{\varphi}$ -direction  $\theta_{\hat{\varphi}}(n)$ , and the relative Lie curvature vector  $\mathbf{k}_{(\text{Lie})}(n)$  (see Table 1 in Ref. [29], for their expressions).

The radiation field is constituted by a coherent flux of photons traveling along null geodesics in the Kerr geometry. The related stress-energy tensor is [27–30]

$$T^{\mu\nu} = \Phi^2 k^\mu k^\nu, \quad k^\mu k_\mu = 0, \quad k^\mu \nabla_\mu k^\nu = 0, \quad (3)$$

where  $\Phi$  is a parameter linked to the radiation field intensity and  $\mathbf{k}$  is the photon four-momentum field. Splitting  $\mathbf{k}$  with respect to the ZAMO frame, we obtain [27, 28]

$$\mathbf{k} = E(n)[\mathbf{n} + \hat{\mathbf{v}}(k, n)], \quad (4)$$

$$\hat{\mathbf{v}}(k, n) = \sin \beta \mathbf{e}_{\hat{r}} + \cos \beta \mathbf{e}_{\hat{\varphi}}, \quad (5)$$

where  $\hat{\mathbf{v}}(k, n)$  is the photon spatial unit relative velocity with respect to the ZAMOs,  $\beta$  is the angle measured in the ZAMO frame in the azimuthal direction,  $E(n)$  is the photon energy measured in the ZAMO frame, i.e., [27–30]

$$E(n) = \frac{E_p}{N} (1 + bN^\varphi), \quad (6)$$

where  $E_p = -k_t$  is the conserved photon energy along its trajectory. The radiation field is governed by the impact parameter  $b$ , associated with the emission angle  $\beta$ .

The photons of the radiation field are emitted from a spherical surface having radius  $R_\star$  centered at the origin of the Boyer-Lindquist coordinates, and rigidly rotating with angular velocity  $\Omega_\star$ . The photon impact parameter has the following expression [30]

$$b = - \left[ \frac{g_{t\varphi} + g_{\varphi\varphi} \Omega_\star}{g_{tt} + g_{t\varphi} \Omega_\star} \right]_{r=R_\star}, \quad (7)$$

The related photon angle in the ZAMO frame is [30]

$$\cos \beta = \frac{bN}{\sqrt{g_{\varphi\varphi}(1 + bN^\varphi)}}. \quad (8)$$

The parameter  $\Phi$  is given by [30]

$$\Phi^2 = \frac{\Phi_0^2}{\sqrt{\mathcal{R}_{\text{rad}}(r)}}, \quad (9)$$

where  $\Phi_0$  is  $\Phi$  evaluated at the emitting surface and

$$\mathcal{R}_{\text{rad}}(r) = (r^2 + a^2 - ab)^2 - \Delta(b - a)^2. \quad (10)$$

A test particle moves with a timelike four-velocity  $\mathbf{U}$  and a spatial three-velocity with respect to the ZAMOs,  $\boldsymbol{\nu}(U, n)$ , which both read as [27–30]

$$\mathbf{U} = \gamma(U, n)[\mathbf{n} + \boldsymbol{\nu}(U, n)], \quad (11)$$

$$\boldsymbol{\nu} = \nu(\sin \alpha \mathbf{e}_{\hat{r}} + \cos \alpha \mathbf{e}_{\hat{\phi}}), \quad (12)$$

where  $\gamma(U, n) \equiv \gamma = 1/\sqrt{1 - \|\boldsymbol{\nu}(U, n)\|^2}$  is the Lorentz factor,  $\nu = \|\boldsymbol{\nu}(U, n)\|$ ,  $\gamma(U, n) = \gamma$ . We have that  $\nu$  represents the magnitude of the test particle spatial velocity  $\boldsymbol{\nu}(U, n)$ ,  $\alpha$  is the azimuthal angle of the vector  $\boldsymbol{\nu}(U, n)$  measured clockwise from the positive  $\hat{\phi}$  direction in the  $\hat{r} - \hat{\phi}$  tangent plane in the ZAMO frame.

We assume that the radiation test particle interaction occurs through Thomson scattering, characterized by a constant momentum-transfer cross section  $\sigma$ , independent from direction and frequency of the radiation field. The radiation force is given by [27–30]

$$\mathcal{F}_{(\text{rad})}(U)^{\hat{\alpha}} = \sigma [\Phi E(U)]^2 \hat{\mathcal{V}}(k, U)^{\hat{\alpha}}. \quad (13)$$

where the term  $\tilde{\sigma}[\Phi E(U)]^2$  reads as [27–30]

$$\tilde{\sigma}[\Phi E(U)]^2 = \frac{A \gamma^2 (1 + b N^\varphi)^2 [1 - \nu \cos(\alpha - \beta)]^2}{N^2 \sqrt{\mathcal{R}_{\text{rad}}(r)}}. \quad (14)$$

The term  $A = \tilde{\sigma}[\Phi_0 E_p]^2$  is the luminosity parameter, which can be equivalently written as  $A/M = L/L_{\text{EDD}} \in [0, 1]$  with  $L$  the emitted luminosity at infinity and  $L_{\text{EDD}}$  the Eddington luminosity. The terms  $\hat{\mathcal{V}}(k, U)^{\hat{\alpha}}$  are the radiation field components, which are [27–30]

$$\hat{\mathcal{V}}^{\hat{r}} = \frac{\sin \beta}{\gamma[1 - \nu \cos(\alpha - \beta)]} - \gamma \nu \sin \alpha, \quad (15)$$

$$\hat{\mathcal{V}}^{\hat{\phi}} = \frac{\cos \beta}{\gamma[1 - \nu \cos(\alpha - \beta)]} - \gamma \nu \cos \alpha, \quad (16)$$

$$\hat{\mathcal{V}}^{\hat{t}} = \gamma \nu \left[ \frac{\cos(\alpha - \beta) - \nu}{1 - \nu \cos(\alpha - \beta)} \right]. \quad (17)$$

In addition we can also connect  $E(U)$  with  $E(n)$  through the following formula [27–30]

$$E(U) = \gamma E(n)[1 - \nu \sin \psi \cos(\alpha - \beta)]. \quad (18)$$

Collecting all the information together, it is possible to derive the resulting equations of motion for a test particle moving in a 3D space, which are [27–30]

$$\begin{aligned} \frac{d\nu}{d\tau} = & -\frac{1}{\gamma} \left\{ \sin \alpha [a(n)^{\hat{r}} \right. \\ & \left. + 2\nu \cos \alpha \theta(n)^{\hat{r}} \hat{\phi}] \right\} + \frac{\tilde{\sigma}[\Phi E(U)]^2}{\gamma^3 \nu} \hat{\mathcal{V}}^{\hat{t}}, \end{aligned} \quad (19)$$

$$\begin{aligned} \frac{d\alpha}{d\tau} = & -\frac{\gamma \cos \alpha}{\nu} [a(n)^{\hat{r}} + 2\theta(n)^{\hat{r}} \hat{\phi} \nu \cos \alpha \\ & + k_{(\text{Lie})}(n)^{\hat{r}} \nu^2] + \frac{\tilde{\sigma}[\Phi E(U)]^2 \cos \alpha}{\gamma \nu} [\hat{\mathcal{V}}^{\hat{r}} - \hat{\mathcal{V}}^{\hat{\phi}} \tan \alpha], \end{aligned} \quad (20)$$

$$U^{\hat{r}} \equiv \frac{dr}{d\tau} = \frac{\gamma \nu \sin \alpha}{\sqrt{g_{rr}}}, \quad (21)$$

$$U^{\hat{\phi}} \equiv \frac{d\varphi}{d\tau} = \frac{\gamma \nu \cos \alpha}{\sqrt{g_{\varphi\varphi}}} - \frac{\gamma N^\varphi}{N}, \quad (22)$$

$$U^{\hat{t}} \equiv \frac{dt}{d\tau} = \frac{\gamma}{N}, \quad (23)$$

where  $\tau$  is the affine parameter (proper time) along  $\mathbf{U}$ .

## 2.1. Photon impact parameter range

We presented the general relativistic 2D PR effect model by using the 3D formulation to make more clear how to derive the photon impact parameter  $b$  in terms of the emitting surface features  $(R_\star, \Omega_\star)$ , see Eq. (7). In addition, it is important to note that  $b$  cannot assume all values, but it ranges in an interval, because once  $R_\star$  is fixed, we have that  $\Omega \in [\Omega_-, \Omega_+]$ , where

$$\Omega_\pm = \frac{-g_{t\varphi} \pm \sqrt{g_{t\varphi}^2 - g_{\varphi\varphi} g_{tt}}}{g_{\varphi\varphi}}, \quad (24)$$

therefore  $b \in [b_{\min}, b_{\max}]$ , see Ref. [30].

We consider the general configuration, where the emitting surface is disjoint by the compact object surface, representing in the reality the case of a hot corona around a BH, where the emitting surface's angular velocity  $\Omega_\star$  is independent from the compact object spin  $a$ . In the NS case,  $\Omega_\star$  and  $a$  are related, representing thus a sub-case of the BH case, and moreover there are more stringent limits on the  $\Omega_\star$  range (see Ref. [30], for more details).

For the discussion on the  $\Omega_\star$  range, it is important to define the event horizon  $R_H$  and the static limit radii  $R_{SL}$  in the equatorial plane, namely

$$R_H = 1 + \sqrt{1 - a^2}, \quad R_{SL} = 2. \quad (25)$$

In all cases, we require that  $\Omega_\star \geq 0$ . In the Schwarzschild case  $R_H = R_{SL}$ , therefore  $R_\star \in [R_H, \infty]$ ,  $\Omega_- < 0$ , and  $\Omega \in [0, \Omega_+]$  (see Fig. 2 in Ref. [30], for more details); instead in the Kerr case we distinguish two regions (see Fig. 1 and Fig. 2 in Ref. [30], for more details):

- $R_\star \in [2, \infty[$  (outside ergosphere), where  $\Omega_- < 0$ , therefore as in the Schwarzschild case  $\Omega \in [0, \Omega_+]$ . We have three intervals for  $\Omega_\star$ :
  - $\Omega_\star = \Omega_{\text{ZAMO}} \equiv -g_{t\varphi}/g_{\varphi\varphi}$ , we have  $b = 0$ ;
  - $\Omega_\star \in [0, \Omega_{\text{ZAMO}}[$ , we have  $b < 0$ ;
  - $\Omega_\star \in ]\Omega_{\text{ZAMO}}, \Omega_+]$ , we have  $b > 0$ ;
- $R_\star \in [R_H, R_{SL}]$  (inside ergosphere), where  $\Omega_- > 0$ , therefore  $\Omega \in [\Omega_-, \Omega_+]$ . There are more regions for  $\Omega_\star$ , where we have the following behaviors:

- $\Omega_\star = \Omega_{\text{ZAMO}}$ , we have  $b = 0$ ;
- $\Omega_\star \in ]\Omega_{\text{ZAMO}}, \Omega_+]$ , we have  $b > 0$ ;
- $\Omega_\star = \Omega_\infty \equiv -g_{tt}/g_{t\varphi}$ , we have  $|b| = \infty$ . In particular, we have  $\lim_{\Omega_\star \rightarrow \Omega_\pm} b = \mp\infty$ ;
- $\Omega_\star \in [\Omega_-, \Omega_\infty]$ , corresponds to photons emitted with negative (conserved) energy  $E_p < 0$ , which cannot escape from the ergosphere.

It is important to note that in view of the classification of the angular velocity  $\Omega_\star$  in terms of the radius  $R_\star$ , we have that for  $R_\star$  in the ergosphere  $b \in [-\infty, b_{\text{max}}]$ , instead for  $R_\star$  outside the ergosphere we have  $b \in [b_{\text{min}}, b_{\text{max}}]$  (see Fig. 2, for details). In addition for  $R_\star \in ]R_H, 2]$ , the spin  $a \in [\bar{a}, 1]$ , where  $\bar{a}$  is the spin value at which we have  $R_\star = R_H(\bar{a})$ . Indeed, for  $a \in [0, \bar{a}]$ , the related  $R_\star$  lie inside  $R_H$ , which represent not physical configurations.

## 2.2. A-priori indications of chaotic behavior

Before to formally prove that the general relativistic PR effect (in the equatorial plane) admits a chaotic behavior through the Melnikov method, we list a series of indications, which induced us to think about that.

The PR effect borrows as a viscous effect in Newtonian gravity, because the radiation drag force depends linearly from the velocity components [25, 29, 33]. In GR, the radiation pressure and the PR effect becomes one single function, which is relativistically covariant, and it is highly-non-linear in terms of the velocity components [34], due to the coupling with the curved non-linear background. The presence of such dissipative perturbation makes the Kerr geodesic motion non-integrable. Non-linear dissipative dynamics and non-integrability are two strong signs in favor of chaos.

If we consider the classical PR effect equations of motion written in terms of  $u = 1/r$  and the azimuthal angle  $\varphi$ , we obtain the differential equation [25, 29, 33]

$$\frac{d^2 u}{d\varphi^2} + \frac{du}{d\varphi} + u = F\left(\frac{du}{d\varphi}, u, \varphi\right), \quad (26)$$

which represents the equation of motion of a forced harmonic oscillator, where the driven force is given by

$$F\left(\frac{du}{d\varphi}, u, \varphi\right) = \frac{du}{d\varphi} \left[1 + \frac{1}{\varphi} + \frac{2}{u} \frac{du}{d\varphi}\right] + \frac{GM - Ac}{A^2 \varphi^2}. \quad (27)$$

Now, if we consider an orbit close to a circular geodesic in the general relativistic PR effect in Schwarzschild spacetime for a radial radiation field, i.e.,  $b = 0$ , we have [27]

$$r(\tau) = r_0, \quad \nu(\tau) = \nu_K, \quad \alpha_0(\tau) = 0, \quad (28)$$

where  $\nu_K = \sqrt{M/(r_0 - 2M)}$  is the Keplerian velocity. We consider  $\varepsilon = A/M \ll 1$  and we linearize the equations

of motion (19) – (23) around this value, obtaining

$$r(\tau) = r_0 + \varepsilon \sqrt{\frac{r_0^3(r_0 - 3M)}{(r_0 - 6M)^2}} \left[ 2\sqrt{\frac{M}{r_0 - 6M}} \sin(\omega_r \tau) - \cos(\omega_r \tau) - \frac{2M}{\sqrt{r_0^3(r_0 - 3M)}} \tau + 1 \right], \quad (29)$$

where

$$\omega_r = \sqrt{M \frac{r_0 - 6M}{r_0^3(r_0 - 3M)}}, \quad (30)$$

is the radial epicyclic frequency expressed with respect to the proper time  $\tau$ . Also in this case, we find the equation of a forced harmonic oscillator. More in general, this behavior is also confirmed by Fig. 3 in Schwarzschild and Kerr spacetimes. Eventually, we can conclude that *the general relativistic PR effect generally behaves as a forced harmonic oscillator, endowed with a highly-non-linear driven force*, which is the responsible to make the dynamics more complicate, non-integrable, and in the same time it works as the engine to create *resonance effects* [5], which then implies chaotic trajectories.

This dynamical system admits the existence of a critical hypersurface (region where the test particle moves stably), proved to be an attractor [32]. In reality, there are two attractors: one is the critical hypersurface and the other one is the spatial infinity  $r \rightarrow \infty$ . The test particle has two possible destinies: ending its motion on the critical hypersurface or escaping at infinity, with no other possible configuration besides these two. The presence of attractors are good signals of chaotic behavior.

Another important aspect is that in considering linear perturbations  $x_1^\alpha$  to the solution of the PR effect system  $x_0^\alpha$  of the form  $x^\alpha = x_0^\alpha + x_1^\alpha$ , we obtain

$$\begin{aligned} r &= r_0 + r_1(\tau), & \varphi &= \varphi_0 + \varphi_1(\tau), \\ \nu &= \nu_0 + \nu_1(\tau), & \alpha &= \alpha_0 + \alpha_1(\tau). \end{aligned} \quad (31)$$

The PR effect equations (19) – (23) in the Schwarzschild spacetime for a general radiation field, i.e.,  $b \neq 0$ , for small first-order linear perturbations [28], read as

$$\frac{dx_1^\alpha}{d\tau} = C^\alpha{}_\beta x_1^\beta. \quad (32)$$

Diagonalizing the linearized matrix  $C^\alpha{}_\beta$ , it is possible to find its eigenvalues, which are [28]

$$\begin{aligned} \lambda_1 &= \sqrt{\frac{r_0 - 2M}{r_0^3(1 - \nu_0^2)}} (\nu_0^2 - \nu_K^2) \operatorname{sgn}(\sin \beta_0), \\ \lambda_2 &= \lambda_1 + i\tilde{\lambda}, \quad \lambda_3 = \lambda_1 - i\tilde{\lambda}, \quad \lambda_4 = 0, \end{aligned} \quad (33)$$

where

$$\tilde{\lambda} = \frac{\pm \nu_0}{r_0(1 - \nu_0^2)} \sqrt{\nu_0^2 - \nu_K^2 + \frac{(r_0 - 3M)(r_0 - 6M)}{r_0(r_0 - 2M)}}. \quad (34)$$

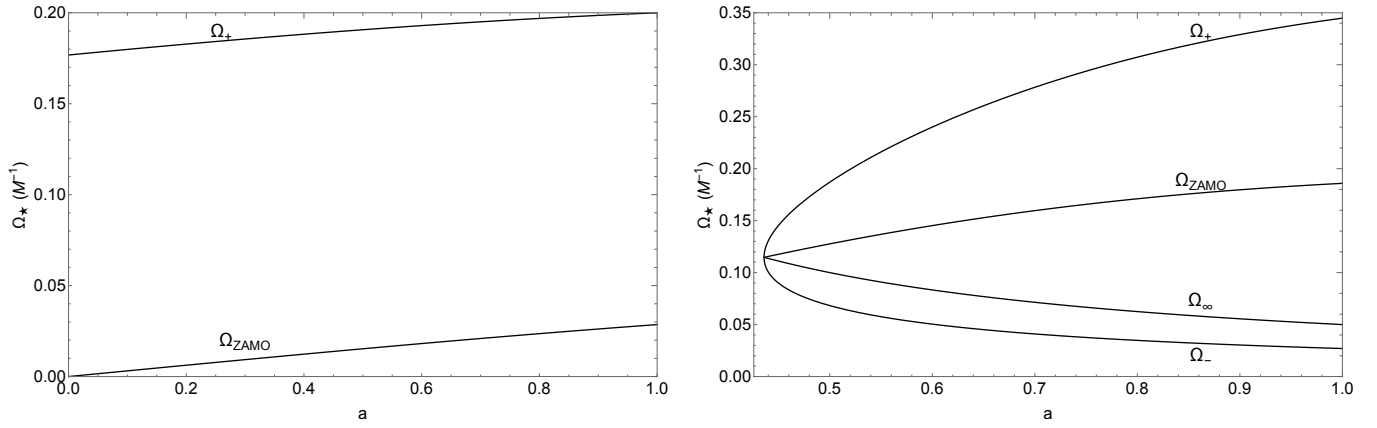


FIG. 1. Emitting surface angular frequency  $\Omega_*$  in terms of the spin  $a$ . Left panel: Plot for  $R_* = 6$ . Right panel: Plot for  $R_* = 1.9$  valid for  $a \in [0.44, 1]$ , because for  $a \in [0, 0.44]$ ,  $R_H \geq 1.9$ . At  $a = 0.44$ ,  $\Omega_* = 0.11$  is the only admitted value.

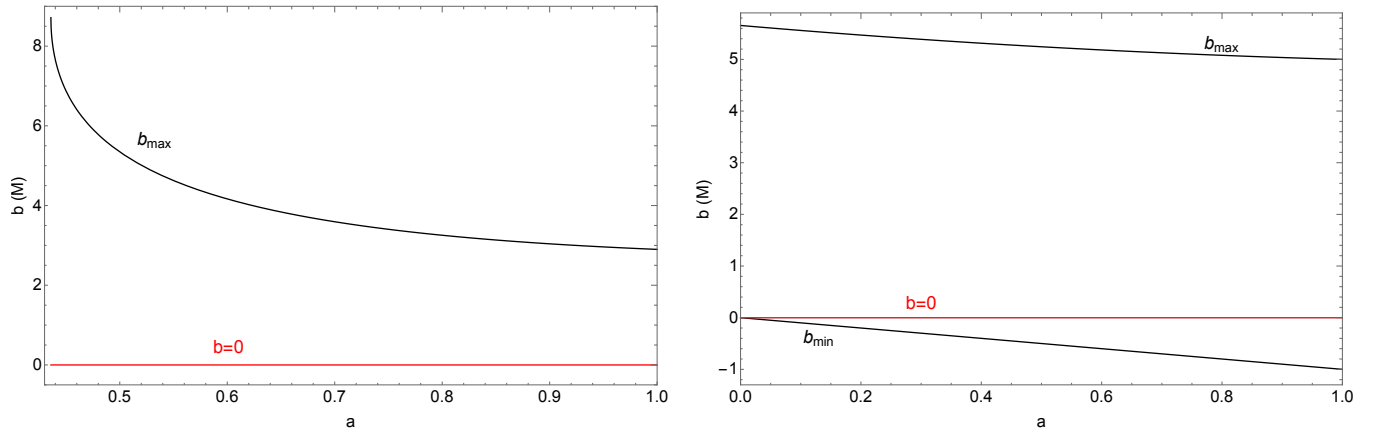


FIG. 2. Photon angular momentum  $b$  in terms of the spin  $a$ . Left panel: Starting at  $a = 0.44$  for  $R_* = 1.9$ , where  $b \in [-\infty, b_{\text{max}}]$ . Right panel: Starting at  $a = 0$  for  $R_* = 6$ , where  $b \in [b_{\text{min}}, b_{\text{max}}]$ .

These eigenvalues assume different values depending on the initial conditions  $(r_0, \nu_0)$ , where the velocity  $\nu_K$  delimits an important threshold. Indeed, we have that  $\lambda_1, \lambda_2, \lambda_3$  are positive in the following cases:

$$\text{if } \text{sgn}(\sin \beta_0) = 1, \quad \Rightarrow \quad \nu_0 > \nu_K, \quad (35)$$

$$\text{if } \text{sgn}(\sin \beta_0) = -1, \quad \Rightarrow \quad \nu_0 < \nu_K. \quad (36)$$

The real parts of  $\lambda_1 = \lambda_2 = \lambda_3$  are positive, their imaginary parts  $\tilde{\lambda} \neq 0$ , and  $\lambda_1$  represents also the *Lyapunov exponent* [5], which measures the mean rate of exponential separation of neighboring trajectories. This is an useful index to see whether a dynamical system shows *sensitive dependence on the initial conditions*, fundamental requirement for exhibiting chaotic dynamics. In Fig. 4, we show different values of  $\lambda_1$  in terms of  $r_0$  and  $\nu_0$ .

### 3. HAMILTONIAN FORMULATION

We have already treated the general relativistic PR effect under a Lagrangian formulation determining the an-

alytical form of the Rayleigh potential through the combination of an integrating factor and the use of a new method called *energy formalism* [33–35].

It is also possible to formulate such effect under an Hamiltonian formalism, never proposed so far in the literature. We here introduce for the first time this formulation, useful for the next calculations.

In the geodesic case, we consider the mass shell constraint with test particle mass  $\mu = 1$ , namely  $g^{\alpha\beta} p_\alpha p_\beta = -1$ , where the momentum canonically conjugate to  $x^\alpha$  occurs through the Legendre transform  $p_\alpha = g_{\alpha\beta} \dot{x}^\beta$ , where the dot stands for the derivative with respect to the affine parameter  $\tau$ . Therefore, the Hamiltonian is

$$\mathcal{H}(\mathbf{p}, \mathbf{x}) = \frac{g^{\alpha\beta} p_\alpha p_\beta}{2}, \quad (37)$$

and, the Hamilton equations are

$$\dot{x}^\mu = \frac{\partial \mathcal{H}}{\partial p_\mu}, \quad \dot{p}_\mu = -\frac{\partial \mathcal{H}}{\partial x^\mu}, \quad (38)$$

which splits a system of  $n$  differential equations of second order (achieved through the Euler-Lagrange equations in



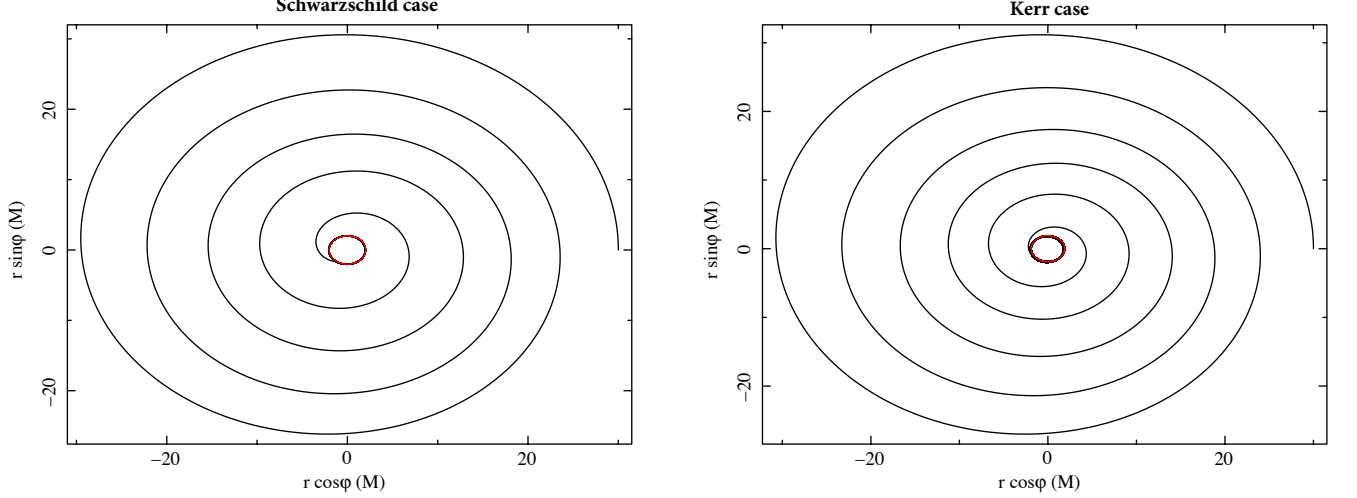


FIG. 3. Test particle orbits in Schwarzschild (left panel) and Kerr  $a = 0.5$  cases (right panel), for  $b = 1$ ,  $A = 0.1$ ,  $(r_0, \nu_0) = (30, 0.18)$ . The red lines represent the critical radii,  $r_{\text{crit}} = 2.02$  (Schwarzschild) and  $r_{\text{crit}} = 1.90$  (Kerr, with  $r_H = 1.87$ ).

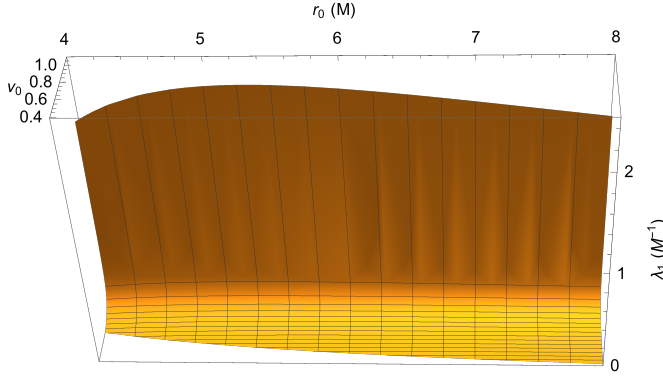


FIG. 4. Lyapunov exponent  $\lambda_1$  plotted in terms of  $r_0$  and  $\nu_0$ .

terms of the Lagrangian  $\mathcal{L}$ ), in  $2n$  differential equations of first order (achieved through the Hamilton equations in terms of the Hamiltonian  $\mathcal{H}$ ). Such formulation can be extended also to a dissipative system  $\mathbf{f} = (f_1^\mu, f_{2,\mu})$ , where the perturbations to the Hamiltonian system can be also of non-Hamiltonian type, having thus

$$\begin{aligned} \dot{x}^\mu &= \frac{\partial \mathcal{H}}{\partial p_\mu} + \epsilon f_1^\mu(\mathbf{p}, \mathbf{x}), \\ \dot{p}_\mu &= -\frac{\partial \mathcal{H}}{\partial x^\mu} + \epsilon f_{2,\mu}(\mathbf{p}, \mathbf{x}), \end{aligned} \quad (39)$$

where  $\epsilon \ll 1$  is a small parameter.

### 3.1. Hamiltonian formulation of the general relativistic PR effect

For the PR effect model, we consider  $x^\mu = (t, r, \varphi)$  the Boyer-Lindquist coordinates and the conjugate momenta read as (see Eqs. (21) – (23), for comparison)

$$p_t = \frac{\gamma}{N}, \quad (40)$$

$$p_r = \sqrt{g_{rr}} \gamma \nu \sin \alpha \sin \psi, \quad (41)$$

$$p_\varphi = \sqrt{g_{\varphi\varphi}} \gamma \nu \cos \alpha \sin \psi. \quad (42)$$

In such formalism, the module of the velocity reads as

$$\nu = \sqrt{\frac{p_r^2}{g_{rr}} + \frac{p_\varphi^2}{g_{\varphi\varphi}}}. \quad (43)$$

The Hamiltonian is simply given by

$$\mathcal{H} = \frac{[g^{tt}p_t^2 + 2g^{t\varphi}p_t p_\varphi + g^{rr}p_r^2 + g^{\varphi\varphi}p_\varphi^2]}{2}. \quad (44)$$

The radiation force components (13) can be written as (see Eqs. (14) – (17), for comparison)

$$\frac{\tilde{\sigma}[\Phi E(U)]^2}{A} = \frac{\gamma^2(1 + bN^\varphi)^2 \mathbb{A}^2}{N^2 \sqrt{\mathcal{R}_{\text{rad}}(r)}}, \quad (45)$$

$$\hat{\mathcal{V}}_{\hat{r}} = \frac{1}{\mathbb{A}} \left( \sin \beta - \frac{p_r}{\sqrt{g_{rr}}} \mathbb{A} \right), \quad (46)$$

$$\hat{\mathcal{V}}_{\hat{\varphi}} = \frac{1}{\mathbb{A}} \left( \cos \beta - \frac{p_\varphi}{\sqrt{g_{\varphi\varphi}}} \mathbb{A} \right), \quad (47)$$

$$\hat{\mathcal{V}}_{\hat{t}} = \frac{1}{\mathbb{A}} \left( \frac{1}{\gamma} - \mathbb{A} \right), \quad (48)$$

where

$$\mathbb{A} = \left[ \gamma - \frac{p_r}{\sqrt{g_{rr}}} \sin \beta - \frac{p_\varphi}{\sqrt{g_{\varphi\varphi}}} \cos \beta \right]. \quad (49)$$

Therefore, we obtain

$$\tilde{F}_\mu = \tilde{\sigma} [\Phi E(U)]^2 \frac{D}{A} \hat{\mathcal{V}}_\mu, \quad (50)$$

where  $D$  is a constant such that  $\epsilon = A/D \ll 1$  (for example  $D = 10$ , so  $\epsilon \in [0.01, 0.1]$ ). The PR effect is a dissipative system, where  $(f_1^\mu, f_{2,\mu}) = (0, \tilde{F}_\mu)$ . Therefore, Eqs. (39) applied to Eqs. (19) – (23) become

$$\dot{p}_r = \frac{\partial_r g_{rr}}{2g_{rr}^2} p_r^2 - \gamma^2 \sqrt{g_{rr}} a(n)^{\hat{r}} \quad (51)$$

$$-k_{(\text{Lie})}(n)^{\hat{r}} p_\varphi^2 \frac{\sqrt{g_{rr}}}{g_{\varphi\varphi}} - 2\gamma p_\varphi \theta(n)^{\hat{\varphi}} \sqrt{\frac{g_{rr}}{g_{\varphi\varphi}}} + \epsilon \tilde{F}_r,$$

$$\dot{p}_\varphi = \epsilon \tilde{F}_\varphi, \quad (52)$$

$$\dot{p}_t = \epsilon \tilde{F}_t, \quad (53)$$

$$\dot{r} = g^{rr} p_r, \quad (54)$$

$$\dot{\varphi} = g^{\varphi\varphi} p_\varphi + g^{t\varphi} p_t, \quad (55)$$

$$\dot{t} = g^{tt} p_t + g^{t\varphi} p_\varphi. \quad (56)$$

As already pointed out in Ref. [36], it arises a spontaneous issue related with the *time*, which is a coordinate in a relativistic phase space. It is responsible thus to make the orbits not recurrent and unbounded in their forward motion. In GR, as we already know, the time loses its absolute meaning as that had in Newtonian gravity. Therefore, to speak coherently about dynamical system in GR [37], we need to split the spacetime through a foliation in spacelike hypersurface, which here occurs through the *relativity of observer splitting formalism* [29, 30, 33].

#### 4. HOMOCLINIC ORBITS

Homoclinic orbits are common concepts in the dynamical systems literature, better known in the BH and gravitational wave literature as *separatrices*, because they permit to distinguish whether the orbits plunge to the horizon or not. The notion of homoclinic orbits is based on the research of *recurrent invariant sets*  $\Lambda$  for a dynamical system [2, 8]. Such sets constitute a collection of points, where the belonging orbits remain in such set at any past or future time. In the phase space, they are normally identified with recurrence properties, like: fixed points, periodic orbits, or the  $n$ -dimensional tori.

The set of all trajectories that approach  $\Lambda$  asymptotically in the infinite future is a submanifold of the phase space termed *stable manifold* of  $\Lambda$ ,  $W^s(\Lambda)$ ; while all trajectories approaching  $\Lambda$  asymptotically in the infinite past represent the *unstable manifold* of  $\Lambda$ ,  $W^u(\Lambda)$ .

An invariant set  $\Lambda$  is called *hyperbolic*<sup>1</sup> if it has both a stable  $W^s(\Lambda)$  and an unstable manifold  $W^u(\Lambda)$ . Now, when the trajectory approaches the same invariant set  $\Lambda$  in the infinite future and past, i.e., if there is an intersection of the stable and unstable manifolds of the same set  $\Lambda$ ,  $W^u(\Lambda) \cap W^s(\Lambda) \cap \Lambda \neq \emptyset$ , then the trajectory is homoclinic (or saddle-loop) to  $\Lambda$ . Formally, the homoclinic orbit approaches the same invariant set in the infinite future as in the infinite past [2, 8]. *Therefore, for determining the class of homoclinic orbits related to a dynamical system relies on identifying the intersections of the stable and unstable manifolds on its hyperbolic invariant sets.*

##### 4.1. Homoclinic orbits in the equatorial plane of Kerr spacetime

We consider the dynamical system given by the Kerr equatorial orbits, governed only by gravity and no other perturbing effects. We will show that the only hyperbolic invariant sets with associated homoclinic orbits are the energetically bounded, unstable circular orbits [36].

The motion of a timelike test particle in Kerr metric in the equatorial plane is given by [38]

$$\dot{r} = \pm \frac{\sqrt{R(r)}}{r^2}, \quad (57)$$

$$\dot{\varphi} = \frac{1}{r^2} \left[ \frac{a}{\Delta} (2rE - aL_z) + L_z \right], \quad (58)$$

$$\dot{t} = \frac{1}{r^2} \left[ \frac{(r^2 + a^2)^2 E - 2arL}{\Delta} - a^2 E \right], \quad (59)$$

where  $E = -p_t$  and  $L_z = p_\varphi$  are the conserved energy and the angular momentum orthogonal to the equatorial plane along the test particle trajectory. It is important to not confuse such constants of motion with those related to the null geodesics of the radiation field,  $-k_t = E_p$  and  $k_\varphi = L_{z,p}$ . The dot stands for the derivative with respect to the affine parameter  $\tau$  along the timelike test particle trajectory. The signs  $\pm$  in front of the radial coordinate (57) mean throughout all the paper that we can consider prograde or retrograde orbits, respectively. The function  $R(r)$  is given by [36, 38]

$$R(r) = r \left\{ -(1 - E^2)r^3 + 2r^2 - [a^2(1 - E^2) + L_z^2]r + 2(aE - L_z)^2 \right\}, \quad (60)$$

In the equatorial Kerr system, the invariant sets are given by the circular orbits (defined by the conditions  $R(r) = 0$  and  $dR(r)/dr = 0$ ); the hyperbolic invariant sets coincide with the unstable circular orbits (defined by circular orbit condition, and  $d^2R(r)/dr^2 < 0$ , which corresponds

<sup>1</sup> The given definition is easily understandable from a plot in the phase space. However, the mathematical definition of an hyperbolic point  $p$  for a  $C^1$  vector field  $\mathbf{F} : \mathbb{R}^n \rightarrow \mathbb{R}^n$ , is:  $p$  is a critical point for  $\mathbf{F}$ , i.e.,  $\mathbf{F}(p) = 0$ , and the Jacobian matrix of  $\mathbf{F}$  at  $p$ ,  $\mathbf{J} = (\nabla \mathbf{F})(p)$ , has no eigenvalues with zero real parts [2, 8].

to the maximum of  $dR/dr = 0$ ). Among these trajectories, the homoclinic orbits are the unstable circular orbits energetically bounded ( $E < 1$ ), see Ref. [36] for details.

In general the equatorial orbits in Kerr metric are described by  $(E, L_z)$ , but however there is another way to define them, which is through the periastron and apastron  $(r_p, r_a)$ . However, since the homoclinic orbits are defined by one-to-one correspondence with bound energy values  $E < 1$ , they constitute a one-parameter family specified by the (periastron) radius  $r_u = r_p$  [36].

It is important to note that the homoclinic orbits have the same energy and angular momentum of the circular orbit they asymptotically approach, and  $E$  and  $L_z$  can be recasted as function of  $r_u$ , i.e., [36, 39]

$$E = \frac{r_u^{3/2} - 2r_u^{1/2} \pm a}{r_u^{3/4} \sqrt{r_u^{3/2} - 3r_u^{1/2} \pm 2a}} < 1, \quad (61)$$

$$L_z = \frac{r_u^2 \mp 2ar_u^{1/2} + a^2}{r_u^{3/4} \sqrt{r_u^{3/2} - 3r_u^{1/2} \pm 2a}}. \quad (62)$$

Rewriting the  $R(r)$  function, which has a double root at  $r_u$  for homoclinic orbits, as [36]

$$R(r) = (E^2 - 1)r(r - r_u)^2(r - r_a). \quad (63)$$

Expanding (63) and equating the same powers of  $r$  with Eq. (60), we have  $r_a$  in terms of  $r_u, E, L_z$ , i.e.:

$$r_a = \frac{2(aE - L_z)^2}{r_u^2(1 - E^2)}. \quad (64)$$

Substituting Eqs. (61) – (62) in Eq. (64) we obtain

$$r_a = \frac{2r_u(a \mp \sqrt{r_u})^2}{r_u^2 - 4r_u \pm 4a\sqrt{r_u} - a^2}. \quad (65)$$

Therefore, the one-parameter family of the homoclinic orbits in the equatorial plane of the Kerr spacetime  $\mathcal{O}^{\text{hc}}(r_u)$  is characterized by Eqs. (61), (62), and (65), where the parameter  $r_u$  must vary between the innermost bound circular orbit (IBCO)  $r_{\text{IBCO}}$  and the innermost stable circular orbit (ISCO)  $r_{\text{ISCO}}$ , i.e.,  $r_u \in [r_{\text{IBCO}}, r_{\text{ISCO}}]$  (see Ref. [36], for further details), where

$$Z_1 = 1 + \sqrt[3]{1 - a^2} [\sqrt[3]{1 + a} + \sqrt[3]{1 - a}], \quad (66)$$

$$Z_2 = \sqrt{3a^2 + Z_1^2}, \quad (67)$$

$$r_{\text{IBCO}} = 3 + Z_2 \mp \sqrt{(3 - Z_1)(3 + Z_1 + 2Z_2)}, \quad (68)$$

$$r_{\text{ISCO}} = 2 \mp a + 2\sqrt{1 \mp a}. \quad (69)$$

In Fig. 5, we show the region where  $r_u$  can vary and also how this region is intersected by the static limit and event horizon radii, useful for the next considerations. In Fig. 6, we display a homoclinic orbit<sup>2</sup> and its related

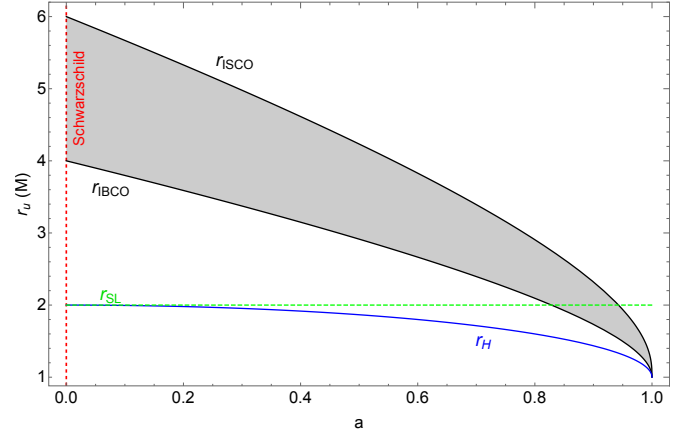


FIG. 5. The shaded area, delimited by IBCO and ISCO radii, is where  $r_u$  can range in terms of the spin  $a$ . The vertical dashed red line represent the Schwarzschild limit ( $a = 0$ ), the horizontal dashed green line is the static limit radius, and the continuous blue line is the event horizon radius.

phase portrait, highlighting in the real space the circular orbit towards which the homoclinic orbit approaches and in the phase space its hyperbolic fixed point.

## 5. MELNIKOV INTEGRAL

The Melnikov method is a powerful mathematical tool to detect the occurrence of chaos in a class of dynamical systems under Hamiltonian periodic perturbations [8], non-Hamiltonian perturbations [2] in two-dimensional and even higher-dimensional systems [40, 41].

To understand how this method is able to identify chaos, it is important to proceed in stages, presenting first simple and abstract examples of chaotic dynamics until to connect all of them to realistic situations occurring in Hamiltonian dynamical systems (see Ref. [14], for a pedagogical introduction to the Melnikov method).

The Melnikov method relies on the following closely connected key-points:

- *baker's transformation*: it is an highly-idealized map from the unit square  $S$  into itself, where  $S$  is cut in half, and the two halves are stacked on one another, and compressed. Using the dyadic decomposition of this map in symbolic dynamics it is possible to prove that it represents the *shift operator*, which is a chaotic map;
- *Smale horseshoe's transformation*: it is another abstract map from the unit square  $S$  into itself, whose action consists in geometrically squishing  $S$ , then stretching the result into a long strip, and finally folding the strip into the shape of a horseshoe inside a unit square  $S$ . It is possible to show that in symbolic dynamics this map is isomorph to the baker's transformation, being thus chaotic;

<sup>2</sup> To plot the homoclinic orbit in the equatorial plane of Kerr metric, we use Eq. (26c) in Ref. [36] for describing the azimuthal coordinate  $\varphi$ , while the radial coordinate  $r$  ranges in  $[r_u, r_a]$ .



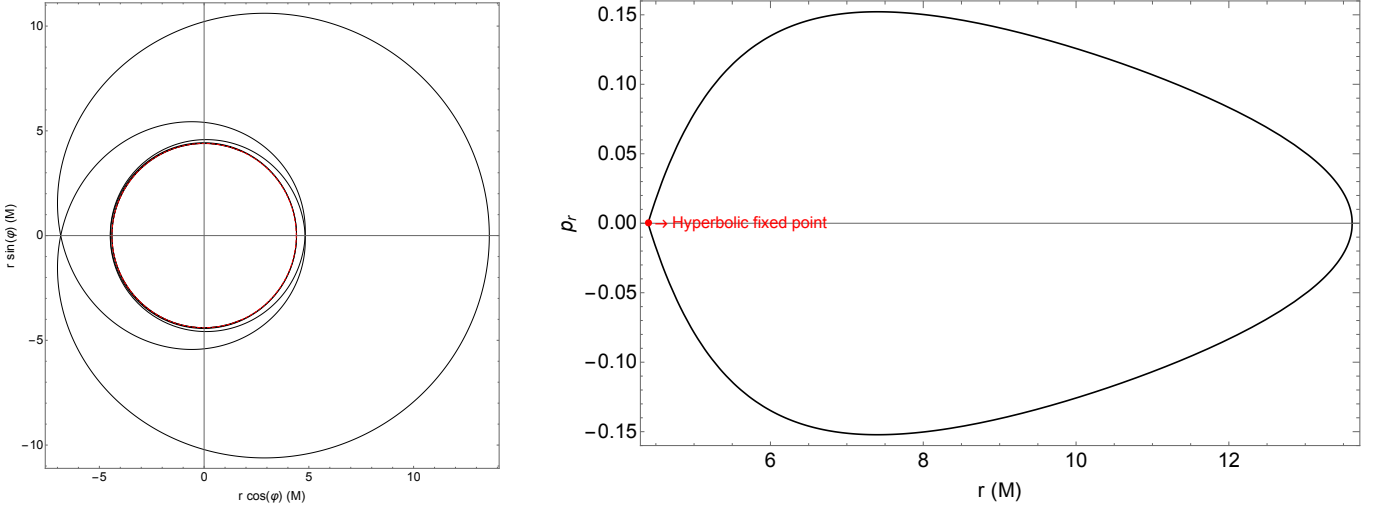


FIG. 6. Homoclinic orbit (left panel) and its phase portrait (right panel), for  $a = 0.1$ ,  $r_u = 4.40$ . The other parameters are  $r_a = 13.61$ ,  $E = 0.95$ , and  $L_z = 3.52$ . The red dashed line represents the circular orbit of radius  $r_u$  centered in  $(0, 0)$  towards which the homoclinic orbit moves. The hyperbolic fixed red point in the phase space is  $(r, p_r) = (r_u, 0)$ .

- *homoclinic tangles*: we consider a map  $\Psi : \mathbb{R}^n \rightarrow \mathbb{R}^n$ , which has an hyperbolic fixed point  $P$ . In Fig. 7, we have drawn an example of homoclinic tangle, useful for its presentation. Then, we define the

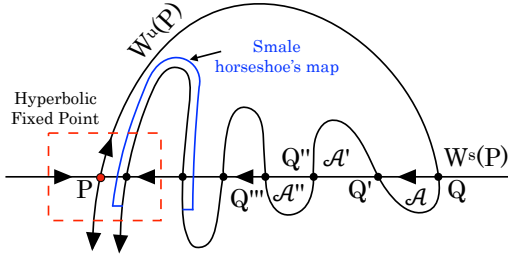


FIG. 7. Example of homoclinic tangle.

stable  $W^s(P)$  and unstable  $W^u(P)$  manifolds of  $P$ :

$$\begin{aligned} W^s(P) &= \left\{ Q \in \mathbb{R}^n \mid \lim_{n \rightarrow \infty} \Psi^n(Q) = P \right\}, \\ W^u(P) &= \left\{ Q \in \mathbb{R}^n \mid \lim_{n \rightarrow -\infty} \Psi^n(Q) = P \right\}, \end{aligned} \quad (70)$$

where

$$\Psi^{\pm n}(Q) \equiv \overbrace{\Psi^{\pm} \circ \Psi^{\pm} \circ \dots \circ \Psi^{\pm}}^n(Q). \quad (71)$$

Since the system  $\Psi$  gives rise to a discrete dynamics,  $W^s(P)$  and  $W^u(P)$  intersect each other only in points, like  $\{Q, Q', Q'', Q''', \dots, P\}$ . In addition, they cannot touch the same point twice, otherwise they will be trapped in a cycle and will not reach the point  $P$ , and  $P$  is not touched in a finite number of steps, since  $P$  is a fixed point (has no image or pre-image of a point other than itself). The intersection of  $W^s(P)$  and  $W^u(P)$  forms the so-called

homoclinic tangles and creates areas  $\mathcal{A}, \mathcal{A}', \mathcal{A}'', \dots$ , which have all the same value, since  $\Psi$  is an area-preserving map. When the two manifolds approach the point  $P$ , they give rise to the Smale horseshoe's map, which permits to imply its chaotic behavior;

- *dissipative Hamiltonian systems*: we consider such kinds of systems, because the general relativistic PR effect model belongs to this category. The unperturbed and integrable Hamiltonian  $\mathcal{H}$  has a fixed hyperbolic point  $P$  in the phase space and  $W^s(P)$  and  $W^u(P)$  coincides in a homoclinic orbit  $\mathcal{O}$ . Such Hamiltonian system is affected by non-Hamiltonian perturbations like Eqs. (39).

We fix an arbitrary initial time  $t_0$  or Poincaré section (where we follow the dynamics) to which corresponds the hyperbolic fixed point  $P_{t_0}$ , the stable  $W^s(P_{t_0})$  and unstable  $W^u(P_{t_0})$  manifolds (see Fig. 8). In order to find

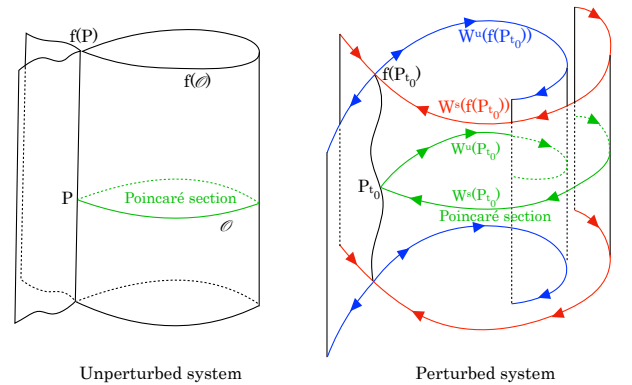


FIG. 8. Sketch to define the Poincaré section.

the homoclinic tangle, we have to determine a way to see

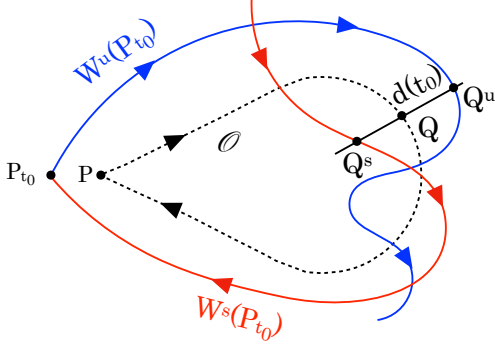


FIG. 9. Sketch to define the Melnikov integral.

when  $W^s(P_{t_0})$  and  $W^u(P_{t_0})$  intersect transversally. We consider a point  $Q \in \mathcal{O}$ , and then we define the distance from  $W^s(P_{t_0})$  to  $W^u(P_{t_0})$  along a direction transversal to  $\mathcal{O}$  in  $Q$ , which intersects  $W^s(P_{t_0})$  and  $W^u(P_{t_0})$  respectively in  $Q^s$  and  $Q^u$ ,

$$d(t_0) \approx \epsilon \frac{\mathcal{M}(t_0)}{\|\nabla \mathcal{H}(P_{t_0})\|} + O(\epsilon^2), \quad (72)$$

where  $\|\nabla \mathcal{H}(P_{t_0})\| \neq 0$  and  $\mathcal{M}(t_0)$  is the Melnikov integral defined as [2, 8, 14, 40, 41]

$$\begin{aligned} \mathcal{M}(t_0) &= \int_{-\infty}^{+\infty} \{\mathcal{H}, \mathbf{f}\} dt \\ &= \int_{-\infty}^{+\infty} \sum_{\mu=1}^n \left( \frac{\partial \mathcal{H}}{\partial p_\mu} f_{2,\mu} + \frac{\partial \mathcal{H}}{\partial x^\mu} f_1^\mu \right) dt, \end{aligned} \quad (73)$$

where  $\{\cdot, \cdot\}$  are the Poisson bracket,  $\mathbf{f}$  are the perturbations of Eqs. (39), and the integral is taken along the unperturbed homoclinic orbit  $\mathcal{O}$ .

Therefore, we arrive to the following conclusions depending on the values assumed by the Melnikov integral:

- $\mathcal{M}(t_0)$  admits odd order zeros, showing thus transversal intersection between  $W^s(P_{t_0})$  and  $W^u(P_{t_0})$ , and therefore homoclinic tangles. The dissipative dynamical systems is chaotic.
- $\mathcal{M}(t_0)$  is bounded away from zero, there is therefore no homoclinic tangle and no chaotic behavior.
- $\mathcal{M}(t_0)$  is identically zero or admits even order zeros, the method cannot predict anything.

### 5.1. Application to the PR effect

We apply the Melnikov method to the general relativistic PR effect (51) – (56), where  $\mathbf{f} = (0, \tilde{F}_\mu)$ . The

Melnikov integral (73) reads as

$$\begin{aligned} \mathcal{M}(t_0) &= \int_{-\infty}^{+\infty} \left[ (g^{tt} p_t + g^{t\varphi} p_\varphi) \tilde{F}_t \right. \\ &\quad \left. + (g^{\varphi\varphi} p_\varphi + g^{t\varphi} p_t) \tilde{F}_\varphi + g^{rr} p_r \tilde{F}_r \right] dt \\ &= \int_{-\infty}^{+\infty} \frac{\tilde{\sigma}[\Phi E(U)]^2 D}{A\mathbb{A}} \left[ (-g^{tt} E + g^{t\varphi} L) \hat{\mathcal{V}}_t \right. \\ &\quad \left. + (g^{\varphi\varphi} L - g^{t\varphi} E) \hat{\mathcal{V}}_\varphi + g^{rr} p_r \hat{\mathcal{V}}_r \right] dt. \end{aligned} \quad (74)$$

This integral is evaluated along the homoclinic orbit  $\mathcal{O} \in \mathcal{O}^{\text{hc}}(r_u)$ , parametrized by the periastron parameter  $r_u$ , being our hyperbolic fixed point  $P$  at the time  $t_0$ . To make more explicit the dependence of the integrating function of Eq. (74) from the homoclinic orbit  $\mathcal{O}$ , we pass from the coordinate time  $t$  to the coordinate radius  $r$  integration, having thus

$$\begin{aligned} \mathcal{M}(t_0) &= 2 \int_{r_u}^{r_a} \frac{\tilde{\sigma}[\Phi E(U)]^2 D}{A\mathbb{A}} \frac{r^2}{\sqrt{R(r)}} \dot{t} \\ &\quad \times \left\{ \left( \frac{\rho}{\Delta} E - \frac{2a}{r\Delta} L_z \right) \left( \frac{1}{\gamma} - \mathbb{A} \right) \right. \\ &\quad \left. + \left[ \frac{(r-2)}{r\Delta} L_z + \frac{2aE}{r\Delta} \right] \left( \cos \beta - \frac{L_z}{\sqrt{\rho}} \mathbb{A} \right) \right. \\ &\quad \left. + \frac{\sqrt{R(r)}}{r^2} \left( \sin \beta - \sqrt{\frac{R(r)}{\Delta}} \frac{\mathbb{A}}{r} \right) \right\} dr \\ &= \int_{r_u}^{r_a} h(r; r_u, a, R_\star, \Omega_\star) \cdot g(r; r_u, a, R_\star, \Omega_\star) dr, \end{aligned} \quad (75)$$

where

$$\begin{aligned} h(r; r_u, a, R_\star, \Omega_\star) &= 2 \frac{\tilde{\sigma}[\Phi E(U)]^2 r D}{A\mathbb{A} \Delta \sqrt{R(r)}} \dot{t}, \\ g(r; r_u, a, R_\star, \Omega_\star) &= \left\{ (r\rho E - 2aL_z) \left( \frac{1}{\gamma} - \mathbb{A} \right) \right. \\ &\quad \left. + [(r-2)L_z + 2aE] \left( \cos \beta - \frac{L_z}{\sqrt{\rho}} \mathbb{A} \right) \right. \\ &\quad \left. + \frac{\Delta \sqrt{R(r)}}{r} \left( \sin \beta - \sqrt{\frac{R(r)}{\Delta}} \frac{\mathbb{A}}{r} \right) \right\}. \end{aligned} \quad (76)$$

To see whether the general relativistic PR effect is a chaotic dynamical system, we have to find the zeros of the  $h \cdot g$  function for  $r \in [r_u, r_a]$ . Regarding the  $h$  function, we numerically checked that the  $R(r)$  function, Eq. (60), does not vanish for any parameter sets; the  $\mathcal{R}_{\text{rad}}(r)$  function, Eq. (10), can vanish for some parameter sets, which are generally in correspondence to some zeros of the  $g$  function, but do not considerably compromise the existence of the chaotic behavior. Instead, the  $\dot{t}$  function can give further simple zeros, but in general they are in correspondence of those of the  $g$  function. Therefore, we can conclude that everything mainly reduces to determine the zeros of the  $g$  function. This analysis cannot be carried out analytically for all parameter sets, due to

non-linear dependence of the  $g$  function from its parameters. Therefore, only a numerical treatment seems to be a viable resolution approach.

We define  $\mathcal{S}$  as the parameter space, namely

$$\mathcal{S} = \{ a \in [0, 1], \quad r_u \in [r_{\text{IBCO}}(a), r_{\text{ISCO}}(a)], \quad R_\star \in ]R_H(a), \infty[, \quad \Omega_\star \in [\Omega_-, \Omega_+] \}. \quad (77)$$

We call *chaotic region*  $\mathcal{C}$  in the parameter space  $\mathcal{S}$ , the set of all parameters  $\{a, r_u, R_\star, \Omega_\star\}$  which annihilates the  $g$  function in terms of the radial coordinate  $r$ , namely

$$\mathcal{C} = \{ (a, r_u, R_\star, \Omega_\star) \in \mathcal{S} / \exists r \in [r_u, r_a(a, r_u)] : g(r; r_u, a, R_\star, \Omega_\star) = 0 \}. \quad (78)$$

In the next section, we discuss how to numerically estimate the chaotic region  $\mathcal{C}$ .

## 6. DISCUSSIONS

The parameters from which the  $g$  function depends are  $a, r_u, R_\star, \Omega_\star$ , because  $a$  determine the proprieties of the background spacetime,  $r_u$  the homoclinic orbit, and  $R_\star, \Omega_\star$  define the photon impact parameter  $b$  and thus the proprieties of the perturbing radiation field. These parameters range in the following intervals, already determined in the previous sections, which can be divided in two parts depending on the values assumed by  $R_\star$  (see Sec. 2.2.1 and Figs. 1, 2, and 5, for more details):

- for  $R_\star \in ]R_H(a), 2]$  (inside the ergosphere)

$$\begin{aligned} a &\in [0, 1], \quad r_u \in [r_{\text{IBCO}}(a), r_{\text{ISCO}}(a)], \\ \Omega_\star &\in [\Omega_-(a, R_\star), \Omega_+(a, R_\star)], \\ b(R_\star, \Omega_\star) &\in [-\infty, b_{\text{max}}(R_\star, \Omega_+)] \end{aligned} \quad (79)$$

- for  $R_\star \in ]2, \infty[$  (outside the ergosphere)

$$\begin{aligned} a &\in [\bar{a}, 1], \quad r_u \in [r_{\text{IBCO}}(a), r_{\text{ISCO}}(a)], \\ \Omega_\star &\in [\Omega_-(a, R_\star), \Omega_+(a, R_\star)], \\ b(R_\star, \Omega_\star) &\in [b_{\text{min}}(R_\star, \Omega_-), b_{\text{max}}(R_\star, \Omega_+)], \end{aligned} \quad (80)$$

while the radial coordinate in  $r \in [r_u, r_a(a, r_u)]$ , for  $R_\star$  both inside and outside the ergosphere.

The emitting surface radius  $R_\star$  together with the spin parameter  $a$  are fundamental in determining the ranges of the other parameters. We note also that the luminosity parameter values  $A$  (different from zero) do not have any influence in determining the chaos regions, rather it is more important the way on how the photons are emitted from the radiation source, namely the value of their impact parameters  $b$ .

In general, once the set of parameters  $\{a, r_u, R_\star, \Omega_\star\}$  has been assigned, the  $g$  function can be plotted in terms of  $r \in [r_u, r_a]$ , and can be checked numerically its behavior. The chaotic region  $\mathcal{C}$  in the parameter space  $\mathcal{S}$

cannot be determined analytically due to non-linear dependence of  $g$  from the parameter set. However, through the plot of several different configurations in  $\mathcal{S}$ , we have collected the following information useful for providing a numerical estimation of the chaotic region  $\mathcal{C}$ .

- For  $R_\star \in ]2, \infty[$  (outside the ergosphere), we have:
  - $g$  does not significantly depends on  $R_\star$ ;
  - $g$  shows simple zeros for almost all values of  $a$ , namely  $a \in [0, \sim 0.9]$ <sup>3</sup>;
  - $g$  shows simple zeros for  $r_u \in [\sim \bar{R}, r_{\text{ISCO}}(a)]$ , where  $\bar{R} = r_{\text{IBCO}}(a) + \frac{1}{5}[r_{\text{ISCO}}(a) - r_{\text{ISCO}}(a)]$ ;
  - $g$  shows simple zeros for  $\Omega_\star$  in intervals depending on the values assumed by  $r_u$ , i.e.,

$$\begin{cases} r_u \sim \bar{R} & \Rightarrow \Omega_\star \in [0, \Omega_+], \\ r_u \in ]\sim \bar{R}, \sim 3\bar{R}] & \Rightarrow \Omega_\star \in [0, \frac{4}{5}\Omega_+], \\ r_u \in ]\sim 3\bar{R}, \sim r_{\text{ISCO}}(a)[ & \Rightarrow \Omega_\star \in [\frac{1}{2}\Omega_+, \frac{7}{10}\Omega_+]. \end{cases} \quad (81)$$

In Fig. 10, we show in few plots the information summerised in this point.

- For  $R_\star \in ]R_H(a), 2]$  (inside the ergosphere), we have detected the following behavior:
  - $g$  significantly depends on the values of  $R_\star$ ;
  - $g$  shows simple zeros for some values of  $a$ , namely  $a \in [\bar{a}, \sim 0.8]$ ;
  - $g$  shows simple zeros for  $r_u \in [\bar{R}, r_{\text{ISCO}}(a)]$ ;
  - $g$  shows simple zeros for  $\Omega_\star$  in intervals not very easy to define. Set  $\bar{\Omega} = \Omega_- + \frac{1}{5}(\Omega_+ - \Omega_-)$ , we have found the following classification:

$$\begin{cases} r_u \sim \bar{R} & \Rightarrow \Omega_\star \in [\sim \bar{\Omega}, \Omega_+], \\ r_u \in ]\sim \bar{R}, \sim 2\bar{R}] & \Rightarrow \Omega_\star \in [\sim 2\bar{\Omega}, \Omega_+], \\ r_u \in ]\sim 2\bar{R}, \sim 3\bar{R}] & \Rightarrow \Omega_\star \in [\sim 3\bar{\Omega}, \Omega_+]. \end{cases} \quad (82)$$

In Fig. 11, we display in some plots the information gathered in this part.

It is important to note that also in the Schwarzschild case there is evidence of chaos (see Fig. 12, for more details). In particular in such case, we have only  $R_\star \in ]2, \infty[$ , because  $R_H(0) \equiv R_{SL} = 2$ .

<sup>3</sup> The symbol  $\sim$  means that it should be consider a relatively small neighbor of a value, namely  $\sim 0.9 = (0.9 - \epsilon, 0.9 + \epsilon)$  with  $\epsilon \ll 1$ .

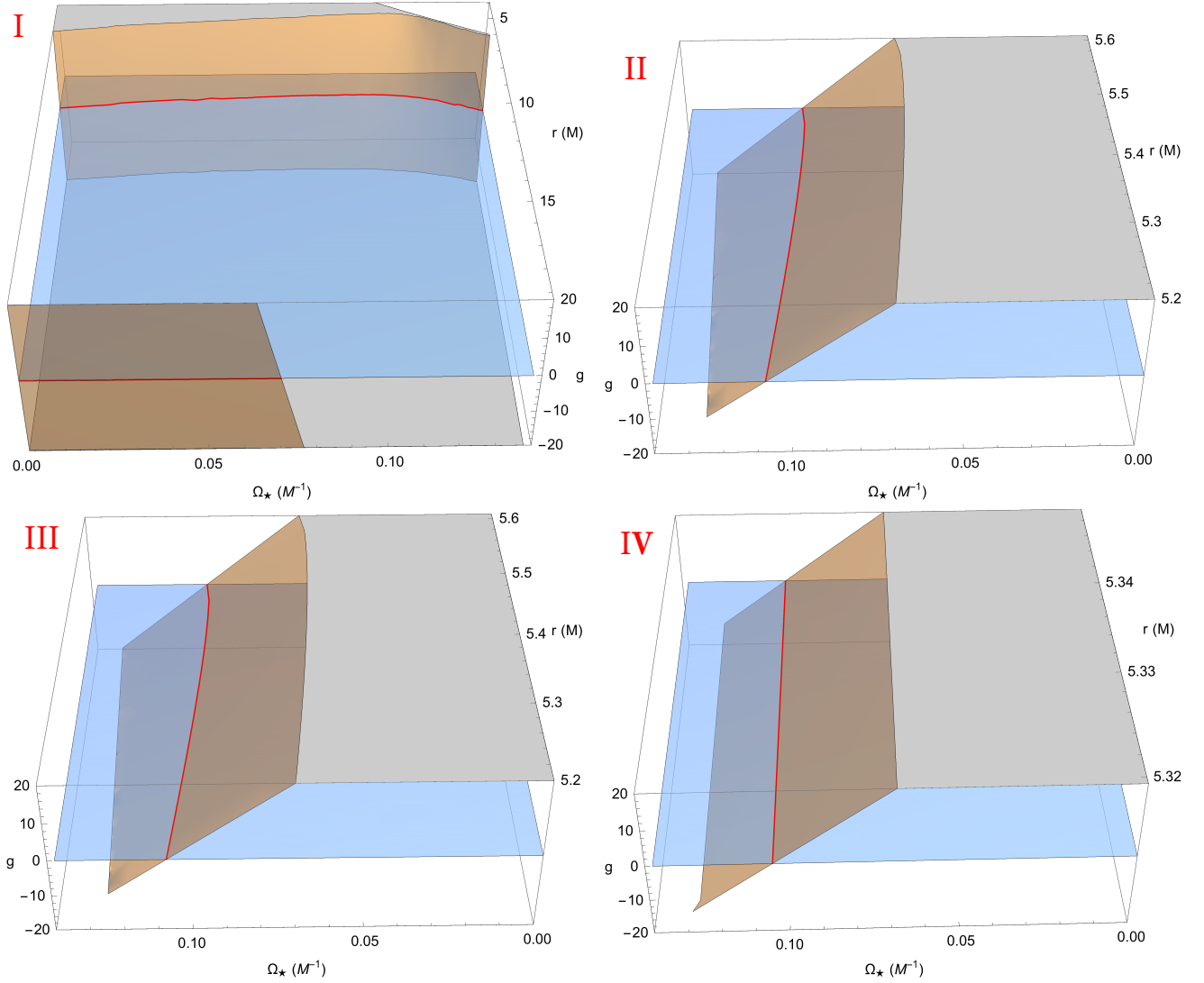


FIG. 10. Plots of the  $g$  function (orange surface) in terms of the radial coordinate  $r$  and the emitting surface angular frequency  $\Omega_*$ . The blue surface represents the “zero” plane, to see for which values of  $r$  the  $g$  function vanishes (red line). The parameters used in these simulations are:  $R_{star} = 6$ , and  $a = 0.2$ . For these values,  $r_u \in [3.59, 5.33]$ , and  $\Omega_* \in [0, 0.14]$ . In each plot, we use a different value of  $r_u$ , namely:  $r_u = 3.94$  (panel I),  $r_u = 4.92$  (panel II),  $r_u = 5.20$  (panel III), and  $r_u = 5.32$  (panel IV).

## 7. CONCLUSIONS

We focused our attention on the general relativistic PR effect in the equatorial plane of Kerr spacetime (see Sec. 2). We then recasted this dynamical system under the Hamiltonian formulation, where the radiation field can be seen as a dissipative non-Hamiltonian perturbation on the pure gravitational Hamiltonian Kerr background (see Sec. 3.3.1). We also introduced the homoclinic orbits in the equatorial plane of Kerr spacetime, which constitute a one parameter family of orbits parametrized by the periastron  $r_u$  (see Sec. 4.4.1).

We took care to define also the intervals where these parameters range, determining thus the parameter space  $\mathcal{S}$ , useful for the next calculations (see Secs. 2.2.1 and 4.4.1). We settled down all the necessary ingredients to

apply the Melnikov method (see Sec. 5) to the general relativistic PR effect on homoclinic orbits in the Kerr equatorial plane, where we determined (see Sec. 5.5.1):

$$g(r; a, r_u, R_*, \Omega_*) = (-g^{tt}E + g^{t\varphi}L)\hat{\mathcal{V}}_t + (g^{\varphi\varphi}L - g^{t\varphi}E)\hat{\mathcal{V}}_{\hat{\varphi}} + g^{rr}p_r\hat{\mathcal{V}}_{\hat{r}}. \quad (83)$$

The  $g$  function does not depend on the luminosity parameter  $A$  (for  $A \neq 0$ , otherwise we have no perturbations), but only from the spin  $a$  (determining the background geometry),  $r_u$  (defining the homoclinic orbit), and  $(R_*, \Omega_*)$  (characterizing the perturbing radiation field).

The  $g$  function vanishes for some parameter sets, which determine the chaotic region  $\mathcal{C}$  in the parameter space  $\mathcal{S}$ . Normally to see whether a system admits a chaotic behavior, one should numerically plot the  $h \cdot g$  function

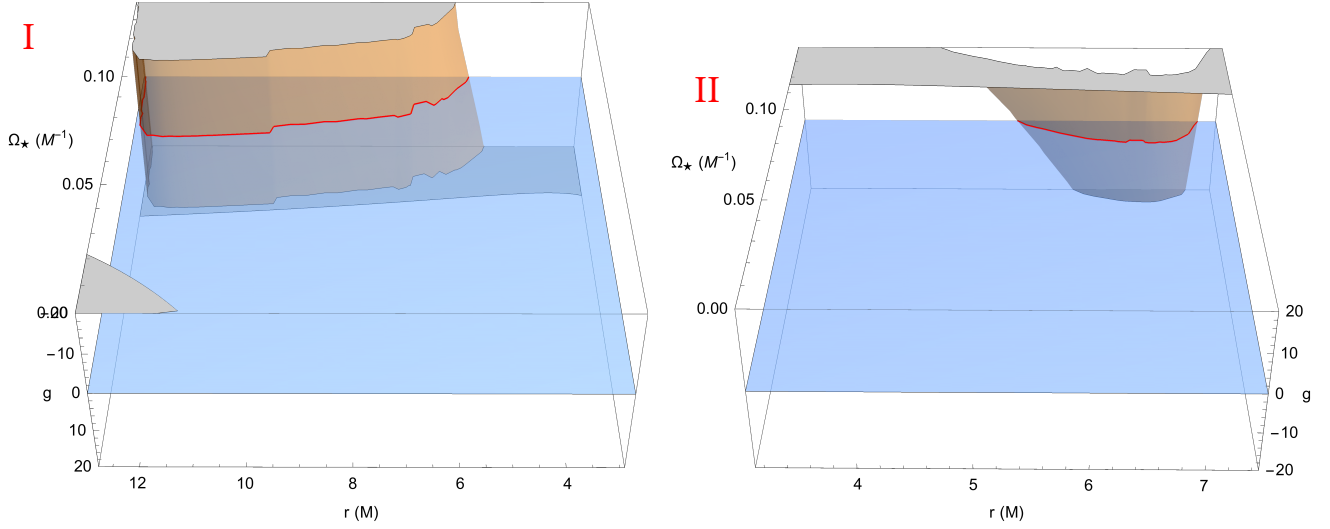


FIG. 11. Plots of the  $g$  function (orange surface) in terms of the radial coordinate  $r$  and the emitting surface angular frequency  $\Omega_*$ . The blue surface and the red line have the same meaning of those in Fig. 10. The parameters used in these simulations are:  $R_{star} = 1.9$ , and  $a = 0.6$ . For these values,  $\bar{a} = 0.44$ ,  $r_u \in [2.66, 3.83]$ , and  $\Omega_* \in [0.50, 0.24]$ . In each plot, we use a different value of  $r_u$ , namely:  $r_u = 2.91$  (panel I), and  $r_u = 3.12$  (panel II).

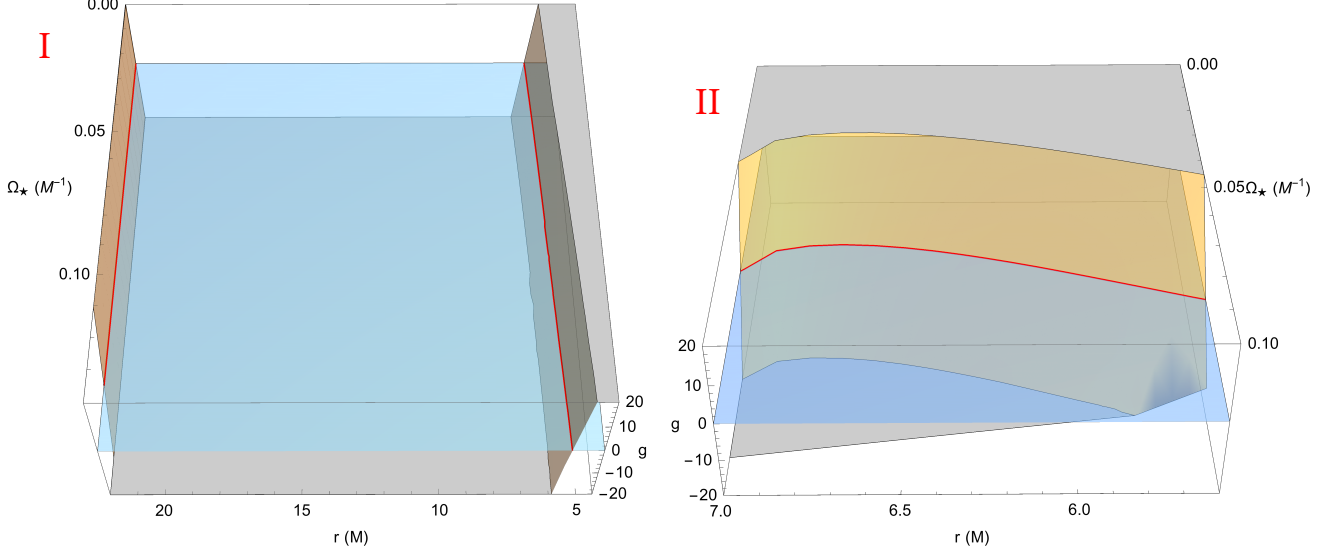


FIG. 12. Plots of the  $g$  function (orange surface) in terms of the radial coordinate  $r$  and the emitting surface angular frequency  $\Omega_*$  for the Schwarzschild case  $a = 0$ . The blue surface and the red line have the same meaning of those in Fig. 10. The parameters used in these simulations are:  $R_* = 4$ ,  $r_u = 4.4$ ,  $\Omega_* \in [0, 0.14]$  (panel I), and  $R_* = 2.1$ ,  $r_u = 5.6$ ,  $\Omega_* \in [0, 0.10]$  (panel II).

(evaluated on the given parameter data set) in terms of the coordinate radius  $r \in [r_u, r_a]$ , and checking whether it admits simple zeros or not (see Sec. 6). We have checked that the  $h$  function does not considerably compromise the existence of the chaotic behavior in terms of the  $g$  function (see Sec. 6, for details).

The chaotic region  $\mathcal{C}$  is not easy to determine analytically, due to the non-linear dependence of the  $g$  function from its parameters. However, performing several numerical simulations, we provided an estimation of it (see Sec.

6). We displayed also some numerical simulations for selected parameter sets, to show some results, see Figs. 10 – 11. We note that also in the Schwarzschild metric it is possible to have a chaotic behavior, see Fig. 12.

There are however some *a-priori* indications that the general relativistic PR effect may show a chaotic behavior: (i) it is a dissipative system that breaks the integrability of the gravitational Kerr spacetime, (ii) the presence of two attractors (critical hypersurface and spatial infinity), (iii) the strong analogy with a forced harmonic



oscillator, where resonance effects can complicate the dynamics, (iv) it shows a sensitive dependence on initial conditions (see Sec. 2.2.2, for more details).

The chaotic behavior of the general relativistic PR effect is an important feature under a dynamical system point of view. This is a fundamental aspect to take into account, especially during the observation process. In addition, the combination of critical hypersurfaces and chaotic motion can be exploited as a valuable tool for lighting up the compact object to a distant observer, as a valuable source of information [42].

The spiraling of astrophysical objects towards super-massive BHs affected by radiation processes can properly collocate within the direct observational detection of gravitational waves (GWs) from the planned LISA mission [43]. In this context, it is fundamental to know the extreme mass ratio inspirals (EMRIs), the astrophysical

information of the system under study, and the underlying dynamics, all valuable information, which contribute to shape the gravitational waveform. In addition, knowing that a system admits chaotic behavior is important, because these configurations can be avoided, otherwise the GW detection cannot succeed. We would like to investigate more deeply such aspects in future works.

Another future prospect is directed towards an extension of such discussion from the equatorial plane to the 3D case always in the Kerr metric, where the treatment of the homoclinic orbits become more complicate [44].

## ACKNOWLEDGEMENTS

The author thanks the Silesian University in Opava and Gruppo Nazionale di Fisica Matematica of Istituto Nazionale di Alta Matematica for support.

- 
- [1] R. Devaney, *An introduction to chaotic dynamical systems* (CRC Press, 2018).
  - [2] S. Wiggins, *Global Bifurcations and Chaos: Analytical Methods*, Applied Mathematical Sciences Series No. v. 73 (Springer-Verlag, 1988).
  - [3] E. Ott, *Chaos in Dynamical Systems* (Cambridge University Press, 2002).
  - [4] M. V. Berry, *Semiclassical Mechanics of regular and irregular motion* (in Les Houches Lecture Series Session XXXVI, eds. G Iooss, R H G Helleman and R Stora, North Holland, Amsterdam, 171-271, 1983).
  - [5] M. Tabor, *Chaos and integrability in nonlinear dynamics: an introduction*, Wiley-Interscience publication (Wiley, 1989).
  - [6] M. Gutzwiller, *Chaos in Classical and Quantum Mechanics*, Interdisciplinary Applied Mathematics (Springer New York, 1991).
  - [7] H. Stöckmann, *Quantum Chaos: An Introduction*, Quantum Chaos: An Introduction (Cambridge University Press, 2006).
  - [8] J. Guckenheimer and P. Holmes, *Nonlinear Oscillations, Dynamical Systems, and Bifurcations of Vector Fields*, Applied Mathematical Sciences (Springer New York, 2002).
  - [9] D. Hobill, A. Burd, and A. Coley, *Deterministic Chaos in General Relativity*, Nato Science Series B: (Springer US, 1994).
  - [10] V. Arnol'd and A. Avez, *Ergodic Problems of Classical Mechanics*, Advanced book classics (Addison-Wesley, 1989).
  - [11] G. Contopoulos, *Proceedings of the Royal Society of London Series A* **431**, 183 (1990).
  - [12] G. Contopoulos, *Proceedings of the Royal Society of London Series A* **435**, 551 (1991).
  - [13] L. F. Wanex, *Chaotic amplification in the relativistic restricted three-body problem*, Ph.D. thesis, UNIVERSITY OF NEVADA, RENO (2002).
  - [14] L. Bombelli and E. Calzetta, *Classical and Quantum Gravity* **9**, 2573 (1992).
  - [15] S. Suzuki and K.-I. Maeda, *PRD* **55**, 4848 (1997), [arXiv:gr-qc/9604020 \[gr-qc\]](#).
  - [16] G. Lukes-Gerakopoulos, in *Fifteenth Marcel Grossmann Meeting - MG15* (2018) pp. 1960–1965, [arXiv:1606.09430 \[gr-qc\]](#).
  - [17] N. J. Cornish, *Phys. Rev. D* **64**, 084011 (2001), [arXiv:gr-qc/0106062 \[gr-qc\]](#).
  - [18] N. J. Cornish and J. Levin, *Phys. Rev. Lett.* **89**, 179001 (2002), [arXiv:gr-qc/0207020 \[gr-qc\]](#).
  - [19] N. J. Cornish and J. Levin, *Phys. Rev. D* **68**, 024004 (2003).
  - [20] J. D. Barrow and H. Sirousse-Zia, *PRD* **39**, 2187 (1989).
  - [21] A. B. Burd, N. Buric, and R. K. Tavakol, *Classical and Quantum Gravity* **8**, 123 (1991).
  - [22] G. Contopoulos, N. Voglis, and C. Efthymiopoulos, *Celestial Mechanics and Dynamical Astronomy* **73**, 1 (1999).
  - [23] E. Calzetta and C. El Hasi, *Classical and Quantum Gravity* **10**, 1825 (1993), [arXiv:gr-qc/9211027 \[gr-qc\]](#).
  - [24] E. Aydiner, *arXiv e-prints*, [arXiv:1610.07338](#) (2016), [arXiv:1610.07338 \[gr-qc\]](#).
  - [25] J. H. Poynting, *Monthly Notices of the Royal Astronomical Society* **64**, 1 (1903).
  - [26] H. P. Robertson, *Monthly Notices of the Royal Astronomical Society* **97**, 423 (1937).
  - [27] D. Bini, R. T. Jantzen, and L. Stella, *Classical and Quantum Gravity* **26**, 055009 (2009), [arXiv:0808.1083 \[gr-qc\]](#).
  - [28] D. Bini, A. Geralico, R. T. Jantzen, O. Semerák, and L. Stella, *Classical and Quantum Gravity* **28**, 035008 (2011), [arXiv:1408.4945 \[gr-qc\]](#).
  - [29] V. De Falco, P. Bakala, E. Battista, D. Lančová, M. Falanga, and L. Stella, *Phys. Rev. D* **99**, 023014 (2019).
  - [30] P. Bakala *et al.*, (2019), [arXiv:1911.00540 \[gr-qc\]](#).
  - [31] M. Wielgus, *MNRAS* **488**, 4937 (2019), [arXiv:1907.11268 \[astro-ph.HE\]](#).
  - [32] V. D. Falco and P. Bakala, (2019), [arXiv:1911.03649 \[hep-th\]](#).

- [33] V. De Falco, E. Battista, and M. Falanga, [Physical Review D \*\*97\*\*, 084048 \(2018\)](#), [arXiv:1804.00519 \[gr-qc\]](#).
- [34] V. De Falco and E. Battista, (in preparation) (2019).
- [35] V. De Falco and E. Battista, [EPL \*\*127\*\*, 30006 \(2019\)](#), [arXiv:1907.13354 \[gr-qc\]](#).
- [36] J. Levin and G. Perez-Giz, [PRD \*\*79\*\*, 124013 \(2009\)](#), [arXiv:0811.3814 \[gr-qc\]](#).
- [37] S. E. Rugh, [arXiv e-prints](#), [gr-qc/9406008 \(1994\)](#), [arXiv:gr-qc/9406008 \[gr-qc\]](#).
- [38] S. Chandrasekhar, *New York : Oxford University Press, 1992.* (1992).
- [39] J. M. Bardeen, W. H. Press, and S. A. Teukolsky, [The Astrophysical Journal \*\*178\*\*, 347 \(1972\)](#).
- [40] P. J. Holmes and J. E. Marsden, [Journal of Mathematical Physics \*\*23\*\*, 669 \(1982\)](#).
- [41] P. J. Holmes and J. E. Marsden, [Communications in Mathematical Physics \*\*82\*\*, 523 \(1982\)](#).
- [42] J. Levin, [Phys. Rev. D \*\*60\*\*, 064015 \(1999\)](#), [arXiv:astro-ph/9811213 \[astro-ph\]](#).
- [43] K. Glampedakis, [Classical and Quantum Gravity \*\*22\*\*, S605 \(2005\)](#), [arXiv:gr-qc/0509024 \[gr-qc\]](#).
- [44] P. Rana and A. Mangalam, [Classical and Quantum Gravity \*\*36\*\*, 045009 \(2019\)](#), [arXiv:1901.02730 \[gr-qc\]](#).